Subtopic: Emissions, Aerosols and Environment

14th U. S. National Combustion Meeting
Organized by the Central States Section of the Combustion Institute
March 16–19, 2025
Boston, MA

Parametric CFD Analysis of Low NOx Combustor Designs for Commercial Supersonic Aircraft

Kumud Ajmani[1,*]
Kathleen M. Tacina[2] *and Thomas R. Luginbuhl*[2]
[1]*Engine Combustion Branch, HX5 LLC, Cleveland OH, USA*
[2]*NASA Glenn Research Center, Cleveland OH, USA*

**Corresponding Author Email: kumud.ajmani-1@nasa.gov*

Abstract: An overview is provided of the impact on NOx emissions of design variations in the six axial airflow Main swirlers of a seven-element lean-direct injection (LDI) module. The CFD study was motivated by the goal of reducing EINOx emissions of a combustor operating at supersonic cruise condition to a nominal value of 10 or below. The Open version of the National Combustion Code (OpenNCC) was used to perform two-phase reacting flow computations with various axial airflow swirler LDI flametube designs with an 'average' Jet-A (A2) fuel. The predicted EINOx emissions for four different air swirler designs were computed with the OpenNCC code were within 25% of each other. The best design in the parametric study showed 20% lower NOx than previous generation LDI injector designs using axial airflow swirlers. Two of the four designs analyzed with the OpenNCC code were down-selected for 3-D manufacturing and testing in NASA Glenn Research Center's CE-13C combustion facility.

1.0 Introduction

In efforts to mitigate the future impacts of using fossil-based aviation fuels on the environment, the aerospace community is investing significant resources into using Sustainable Aviation Fuels (SAFs) in liquid-fueled gas-turbine combustors [1]. While future commercial supersonic aircraft are likely to use high blends of SAF or 100% SAF to reduce life-cycle carbon emissions, in research efforts to design Lower NOx combustors continues to remain high at NASA GRC, injector manufacturers and engine OEMs [2]. Reduction of emissions that impact the environment and human health is a significant research area under NASA's Commercial Supersonic Technology (CST) project.

Commercial supersonic aircraft are projected to spend most of their cruising flight envelope at relatively higher altitudes and higher combustor operating temperatures as compared to current subsonic aircraft. The combination of higher cruise operating temperatures at higher altitudes, combined with the goal of ultra-low NOx emissions, creates unique design challenges for commercial supersonics combustors [3]. In addition to reducing NOx and CO emissions in high-altitude flight, reducing carbon emissions by using SAFs is also a significant research area for commercial subsonic and supersonic aircraft. In recent efforts, NASA Glenn's Open National Combustion Code (OpenNCC) has been used for multiple CFD efforts to guide Lean Direct Injection (LDI) redesigns [4] and study the impacts of SAF fuel blends on emissions [5].

This paper describes a CFD effort focused on redesigning the injector modules of an existing Lean Direct Injection (LDI) combustor, with the goal of attaining an EINOx of 10 or below at supersonic cruise conditions. The CFD study described here focuses on injector redesign to support commercial supersonics flight emissions goals, as compared to two previous CFD studies which focused on evaluating the impacts of fuels on emissions and flame-structure: (a) evaluate impacts of arbitrary fuel blending ratios of 'average' Jet-A (A2) and GEVO Alcohol-to-Jet (ATJ or C1) fuel [5] and (b) evaluate impacts of three different, unblended fuels: 'average' Jet-A (A2), RP-2 and SASOL iso-paraffin kerosene (IPK) [6].

The ‘baseline’ configuration used as a starting point for the current parametric design study was a single cup of a three-cup, third generation LDI combustor (LDI-3). The LDI-3 flametube was designed by Woodward FST Inc, to meet performance and emissions requirements for subsonic aviation under NASA’s N+3 Advanced Air Transport Technology (AATT) program [2]. While this combustor was not optimized for a supersonic aircraft cycle, it provided a realistic starting point to attempt a low-NOx combustor redesign to meet supersonic cruise emissions goals for commercial supersonics. Figure 1 shows a representation of the dome-layout of the three cups of the ‘baseline’ design as tested at NASA GRC. As part of combustion testing at NASA GRC, emissions data were obtained for certain supersonic cycle operating points (cruise, maximum power). Design details of one of the seven-element cups with axially-bladed airflow swirlers used in the six outer (main) elements, and a corresponding mesh for CFD analysis, are also shown in figure 1.

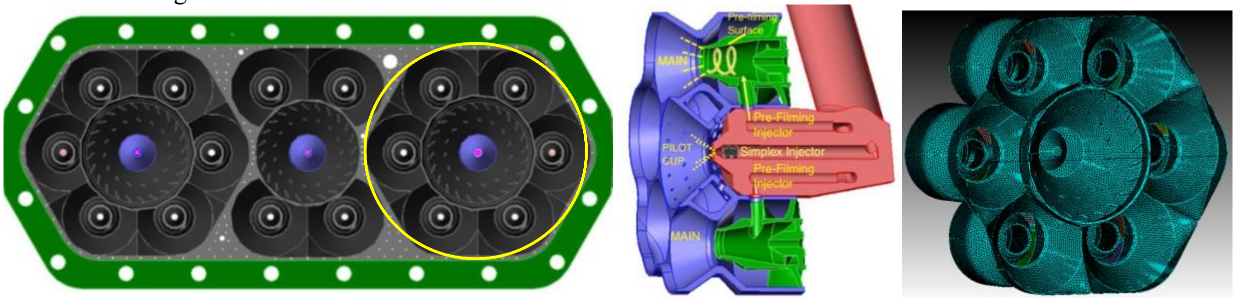

Figure 1. ‘Baseline’ LDI-3 Design: Three-cup dome-layout with alternating seven- and five-element cups for the original LDI-3 injector array (left); details of the ‘axial-bladed’ seven-element cup with six outer mains and center pilot with cooling holes (middle); OpenNCC CFD surface mesh for ‘baseline’ seven-element configuration (right).

The primary design parametric studied with the OpenNCC was the variation in the blade passage angle of the axially bladed swirlers for each of the six main injectors. Two isometric views of the injection elements, along with the partial details of the surface mesh for the CFD configuration, are shown in figure 2. The ‘baseline’ configuration had co-rotating helical passages with a 48° turning angle for each of the outer six main injection elements. The swirler angle variations considered were: 52°, 55° and 60° passages with all co-rotating swirlers in all six main injectors; and a fourth 55° configuration with alternating co- and counter-rotating passages. For this parametric study, the central pilot injector and cooling hole geometry was kept identical for each of the designs evaluated with the OpenNCC.

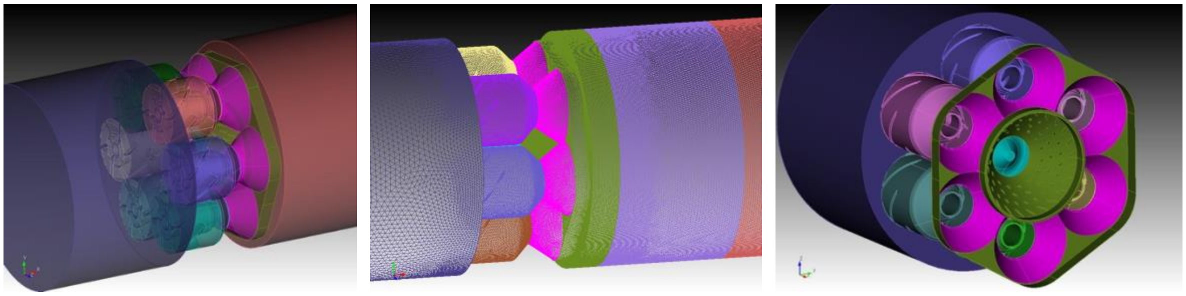

Figure 2. Low NOx Combustor single cup injector: seven-element injector, aft looking forward (left); surface mesh details for CFD (upstream plenum, main injectors, downstream cylindrical section); aft looking upstream showing details of dome face layout

2.0 Parametric CFD Assessment of Injector Redesigns with the OpenNCC

The CFD computations in this study are based on the OpenNCC’s two-equation turbulence model [7], a lagrangian-spray modeling approach for the liquid phase droplets [8] and the gas-phase HyChem reduced-kinetics mechanism of Wang *et al*. [9] for average Jet-A fuel (A2). The computations are performed with an upwind-differencing scheme with second-order accurate discretization for both viscous and inviscid fluxes [10]. An initial steady-state RANS solution is obtained by using an explicit, four-stage Runge-Kutta scheme with smoothing of residuals in pseudo-time to accelerate convergence. The steady-state solution is used as an initial condition to obtain a time-accurate solution using a dual time-stepping approach with a typical physical time-step of 1×10^{-6} s for the second-order time-accurate solver.

2.1 Flamelet Progress Variable Method for OpenNCC

The OpenNCC code has the capability to use a Flamelet Progress Variable combustion model to compute two-phase flow combustion flows for liquid-fueled gas-turbine combustors [11]. The general FPV model has recently been extended to a Multiple Time-Scale method (MTS-FPV) [12] in order to reduce the computational time needed to obtain convergence of emissions calculations, particularly NOx species and particulates in aircraft combustor configurations. A multiphase flamelet progress variable approach is employed for the primary flame and the species responsible for NOx emissions are transported independently as separate scalars. The MTS-FPV approach in the OpenNCC solves transport equations for the mean mixture fraction ($\overline{Z}$), its variance (V_z) and mean progress variable ($\overline{Y}_p$):

$$\frac{\partial}{\partial t}(\bar{\rho}\bar{Z}) + \frac{\partial}{\partial x_i}(\bar{\rho}u_i\bar{Z}) - \frac{\partial}{\partial x_i}[\bar{\rho}(D + D_T)\frac{\partial \bar{Z}}{\partial x_i}] = 0 \qquad (1a)$$

$$\frac{\partial}{\partial t}(\bar{\rho}V_z) + \frac{\partial}{\partial x_i}(\bar{\rho}u_iV_z) - \frac{\partial}{\partial x_i}[\bar{\rho}(D + D_T)\frac{\partial V_z}{\partial x_i}] = \bar{f} \qquad (1b)$$

$$\frac{\partial}{\partial t}\left(\bar{\rho}\overline{Y}_p\right) + \frac{\partial}{\partial x_i}\left(\bar{\rho}u_i\overline{Y}_p\right) - \frac{\partial}{\partial x_i}[\bar{\rho}(D + D_T)\frac{\partial \overline{Y}_p}{\partial x_i}] = \overline{\dot{S}_p} \qquad (1c)$$

where $\bar{f}=2\bar{\rho}(D_T)\frac{\partial \bar{Z}}{\partial x_i}\frac{\partial \bar{Z}}{\partial x_i} - 2\bar{\rho}\frac{V_z}{k}\epsilon$ and $\overline{\dot{S}_p}$ is the source term for the progress variable provided by the flamelet table (please note that the bar means averaged quantities). A table lookup is performed to characterize the thermochemical state of the major species.

In order to extend the FPV approach to support droplet injection of liquid fuel sprays in typical aircraft combustors, the effect of mass addition needs to be accounted for via the implementation of a source term in the mixture fraction equation (1a) as

$$\frac{\partial}{\partial t}(\bar{\rho}\bar{Z}) + \frac{\partial}{\partial x_i}(\bar{\rho}u_i\bar{Z}) - \frac{\partial}{\partial x_i}[\bar{\rho}(D + D_T)\frac{\partial \bar{Z}}{\partial x_i}] = \dot{S}_v \qquad (2)$$

It is emphasized that the mixture fraction equation is no longer conservative and now features a source term due to evaporation of the fuel droplets.

One unique feature of the MTS-FPV implementation in the OpenNCC to speed up emissions calculations is that the primary flame and the species associated with NOx production are decoupled from the primary flame computation. In order to decouple the disparate time-scales of NOx species evolution and accelerate convergence of the stiff equations related to NOx species, the table lookup for the primary flame computation is performed without including the NOx species in the flamelet table. The NOx chemical source terms for the auxiliary transport equations are then evaluated based on the local thermochemical state using a detailed NOx chemical mechanism.

Additional equations for auxiliary progress variables $\overline{Y}_{p,j}$ are solved separately from the primary flame progress variable. For example, if NO, N, NO_2, and N_2O are chosen as the species for NOx computation, four additional equations would be solved as:

$$\frac{\partial}{\partial t}\left(\overline{\rho\,Y}_{p,j}\right) + \frac{\partial}{\partial x_i}\left(\bar{\rho}u_i\overline{Y}_{p,j}\right) - \frac{\partial}{\partial x_i}\left(\bar{\rho}(D + D_T)\frac{\partial \overline{Y}_{p,j}}{\partial x_i}\right) = \overline{\dot{S}_{p,j}} \qquad (3)$$

Such a framework has been shown to accurately capture NOx emissions in a cost-effective manner with the OpenNCC [13] and is extended in this work for soot emissions computations. The current MTS-FPV framework in the OpenNCC allows for any number of user-specified auxiliary progress variable equations to be solved, including those for say, computing soot emissions.

2.2 Chemical Kinetics Modeling for Jet-A Fuel

The chemical modeling approach of the OpenNCC used the Jet-A fuel HyChem skeletal-kinetics mechanism of 41-species [9] for the generation of the flamelet table for use with the Flamelet Progress Variable (FPV) method. Some details of the chemical and combustion properties of average Jet-A fuel (A2), as used in the HyChem kinetics modeling, are shown in Table 2. The CANTERA [14] computed values for flame temperature, ignition delay and flame speed were 1824K, 24.9 m-sec and 32.6 cm/s, respectively. The CANTERA computations were performed for the cruise condition of a supersonic cycle point of interest in this work (P_3= 15.9bar, T_3=884K, phi=0.43), and all three computed values agreed well with experimental data for A2 fuel. All gas-phase thermodynamic and transport properties used for both the CANTERA and OpenNCC's FPV flamelet table were those provided with the 41-species HyChem mechanism. In this study, temperature-dependent physical and transport properties (density, heat capacity, viscosity, vapor pressure, latent heat) for the liquid A2 fuel were based on the work of Esclapez [15].

Table 1. Gas phase and liquid fuel properties for A2 fuel used in OpenNCC

Gas Fuel Property / Kinetics [8]	A2
Chemical Formula (Average)	$C_{11.4}H_{21.7}$
H/C ratio	1.90
Derived Cetane Number (DCN)	47
Net heat of Combustion (MJ/kg)	42.8
Chemical Formula (Modeled)	$C_{11}H_{22}$
Number of Species (Skeletal Kinetics)	41
Adiabatic Flame Temperature, K	1824
Ignition Delay Time, m-sec	24.9
Flame Speed, cm/s	32.6

Liquid Fuel Property	A2
Molecular Weight (g/g-mole)	154.1
Normal Boiling Point (K)	489.5
Density at 1bar (kg/m^3)	791.5
Critical Temperature (K)	760.4
Critical Pressure (bar)	18.2
Heat of Vaporization (kJ/kg)	310.0
Critical Volume (cm^3/g-mole)	700.4

2.3 Spray Modeling for A2 Fuel

The skeletal finite-rate kinetics models for A2 fuel were coupled with OpenNCC's lagrangian-spray liquid-fuel modeling [8] to compute heat release, flame-structure, and emissions for the injector configurations shown in figure 2. The droplet size distribution for injected particles for both the Main and Pilot elements was prescribed by the following correlation equation :

$$\frac{\delta n}{n} = 4.21 \times 10^{6} \left[\frac{d}{d_{32}}\right]^{3.5} e^{-16.98\left[\frac{d}{d_{32}}\right]^{0.4}} \frac{\delta d}{d_{32}} \quad (4)$$

Here n is the total number of droplets, d_{32} is the Sauter mean diameter (SMD), and δn is the number of droplets in the size range between d and $d + \delta d$.

Spray modeling for the main injection elements assumed that the fuel sheet exiting the pre-filming surface broke up into streams of uniform liquid mass and momentum. Each annular sheet of liquid fuel was approximated as a set of 8 discrete fuel streams, located 45^o apart in the circumferential direction and 1mm downstream of the trailing edge of the exit of the pre-filming surface of each injection element. Each stream was modeled as a 5^o-solid cone injected in 8 stochastically varying directions with an SMD (d_{32}) of 8μm with 8 droplet groups (δn) in equation 4. The initial droplet injection velocity and temperature were 5m/s and 300K, respectively. The pressure-atomizing simplex injection element (Pilot) located at the center of the seven-element injector cup was modeled as a 60^o hollow cone of 10^o thickness. Liquid particles were injected as 16 stochastically varying spatial streams at an injection velocity of 28m/s; droplet size and liquid mass distribution was achieved using 8 droplet groups and an SMD of 8μm.

2.4 Meshing and CFD Approach for Low-NOx Designs

Several tetrahedral meshes of increasing mesh densities were generated for the ACS Combustor with LLNL's CUBIT mesh generation software [16]. Non-reacting solutions were computed with OpenNCC for each mesh and the predicted 'effective area' (AC_d) for the Pilot injector and the Main injectors were compared with experimental data. Mesh convergence criteria was achieved when the predicted values of AC_d for the original 48^o design were within 10% of experimental measurements. The tetrahedral mesh for each injection element within a particular blade angle design was an exact copy of each other. In order to minimize mesh variations across the designs, the tetrahedral mesh count for each main injection element was kept within 1% of each other (406,000 elements). The tetrahedral mesh for the Pilot injection element, pilot cooling holes, the upstream plenum and the downstream combustor section was kept identical for each configuration. The final tetrahedral mesh count for each of the four design variations was within 1% of the average mesh count of 14.5 million elements and 2.6 million nodes.

The OpenNCC CFD computations were performed for a supersonic cruise condition of P_3=15.9bar (234psi), T_3=884K (1132F), phi=0.43 (FAR=0.0295), T_4=1840K (2852F) and Δp=3.5%. The airflow inlet boundaries for the Pilot and Main injectors, and the cooling hole inlets, were modeled with fixed total pressure and total temperature conditions derived from the P_3 and T_3 for the cruise condition. The outflow boundary was modeled with a fixed static-pressure for subsonic outflow based on the specified Δp between the inflow and outflow of the combustor. No-slip, adiabatic flow conditions were imposed at all solid surfaces.

An initial, non-reacting flow solution for each of the four injector designs was generated using RANS CFD with a 2nd-order accurate central-differencing operator and 4-stage explicit Runge-Kutta time-integration. The non-reacting RANS solution was then used to generate a time-accurate solution (10000 time-steps at 1e-6s) using a dual-time stepping approach, coupled with the Time-Filtered Navier Stokes (TFNS) solver of OpenNCC. A reacting-flow TFNS computations (41species HyChem kinetics with flamelet table lookup) was then obtained, with initiation of fuel-injection and artificial ignition of the fuel-air mixture downstream of each of the seven injection elements. Reacting flow solutions with four additional auxiliary progress variables for NOx (see eq. 3) were then initiated, and converged solutions for EINOx were obtained for each design.

3.0 OpenNCC CFD Results for Low NOx Injector Redesigns

The CFD predictions of flow aerodynamics, flame-structure and EINOx emissions from the four design variations studied with the OpenNCC were used to down-select two final designs for 3-D printing and combustion testing in NASA Glenn Research Center's CE-13 combustion test facility. The primary design parametric was that of varying the blade angle of the axially bladed swirler passages for the six main injection elements (see fig. 1). The first three variations from the baseline 48° axial swirlers were blade passages with 52°, 55° and 60° swirlers, respectively. A fourth variation with alternating co- and counter-rotating 55° swirlers passages in the six main elements was also analyzed with the OpenNCC. The five criteria used for design down-selection were (a) the total effective area of each seven-element injector cup, (b) the size and stability of the recirculation zones behind the various injection elements, (c) the predicted EINOx for each design, (d) the potential to successfully perform fuel-staging between the Pilot and Main injection elements to reduce EINOx and (e) the flame structure that would potentially allow for the lowest liner cooling flow requirements at the walls of an annular combustor.

3.1 CFD Based Down-selection: Phase 1 (Non-reacting Flow)

The first phase of the CFD-driven down-selection was informed by OpenNCC's non-reacting flow CFD predictions of effective area (AC_d) and recirculation zones for the four different swirler angle configurations of the six main injection elements. A summary of the predicted AC_d values for each design parametric, as normalized by the AC_d of the six injection elements of the 52° design is shown in Table 2. The normalized AC_d values for the Pilot injection element and the four rows of cooling flow holes that cool the Pilot venturi, are also listed in Table 2. As expected, the predicted AC_d value decreases as the Main swirler blade passage angle increases. This can be attributed to increased aerodynamic and viscous losses for the 55° and 60° swirler designs as compared to the 52° design. In order to test the accuracy of the OpenNCC AC_d predictions for the four design variations, the AC_d for the original 48° design was also computed and found to be within 10% of the measured values reported in a previous study [4].

The contours of axial velocity in various cross-sectional slices of the four designs, as created by post-processing of CFD results with VisIt [17] are shown in figure 3. A qualitative comparison of the sizes and strengths of the recirculation zones was used to choose between the two 55° swirler configurations, both of which had almost identical predictions for AC_d values. The 55° alternating swirler design was predicted to have a much shorter and weaker recirculating zone as compared to the 55° co-rotating swirlers, particularly behind the central pilot injector. The aerodynamics of all three co-rotating swirlers (52°, 55° and 60°) were very stable, and also predicted to be very similar to each other. Based on the predictions of effective area, size and stability of their recirculation zones, the three co-rotating 52°, 55° and 60° swirler designs were down-selected for analysis with two-phase reacting flow computations with the OpenNCC.

Table 2. Effective areas (AC_d) of various airflow passages of four different single-cup designs (normalized by the effective area of the six mains elements of the 52° configuration)

Swirler Angle (Six Main Elements)	Normalized Effective Area (Six Mains)	Normalized Effective Area (Pilot)	Normalized Effective Area (Pilot Cooling)
60° (Co-Rotating)	**0.78**	**0.12**	**0.0167**
55° (Co-Rotating)	**0.90**	**0.12**	**0.0167**
55° (Alternating Co- and Counter-Rotating)	**0.89**	**0.12**	**0.0167**
52° (Co-Rotating)	**1.00**	**0.12**	**0.0167**
48° (Original design, Co-Rotating)	**1.11**	**0.12**	**0.0167**

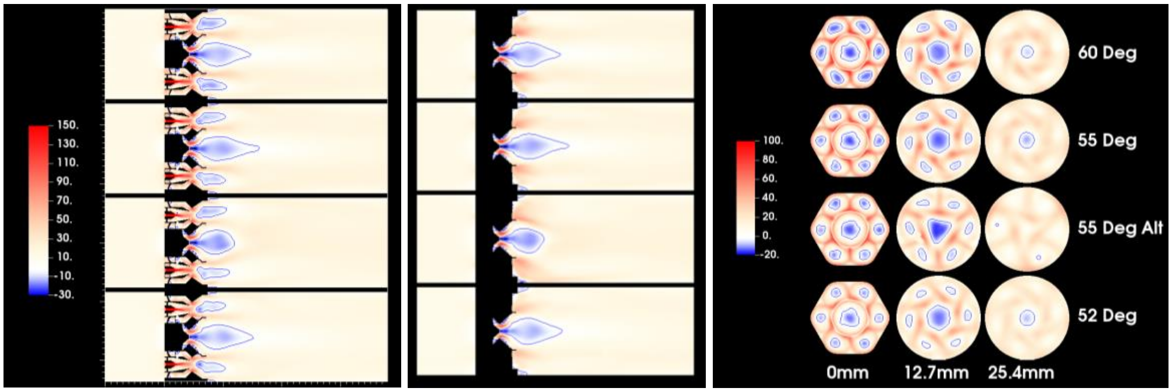

Figure 3. OpenNCC contours of axial flow velocity (m/s). **Left**: pilot and two mains mid-pane. **Center**: pilot only mid-plane. **Right**: three axial cross-sections at 0mm (combustor dome), 12.7mm and 25.mm

3.2 CFD Based Down-selection: Phase 2 (Two-Phase Reacting Flow)

The second phase of the parametric CFD study with OpenNCC focused on two-phase reacting flow computations for the three designs down-selected based on the initial non-reacting flow CFD predictions of effective area and flow aerodynamics, and the original single-cup design with 48° swirlers for the six main elements. Details of the MTS-FPV flamelet table lookup approach with auxiliary progress variable equations for NOx species, the reduced chemical kinetics mechanism and the lagrangian spray model of OpenNCC used for the reacting flow CFD predictions were previously described in sections 2.1, 2.2 and 2.3, respectively.

A comparison of reacting flow velocity profiles in a mid-plane section for each of the four swirler angle configurations is shown in figure 4. The heat release of combustion considerably impacts the size and strength of the recirculation zones behind each injection element, as compared to the non-reacting flow predictions (see fig. 3). The predicted CFD recirculation zones for each of the three design variations are qualitatively similar to each other and to the original 48° swirler design. All four designs show relatively weaker recirculation zones behind the mains and stronger recirculation behind the central pilot, as the swirler angle decreases. The net aerodynamic effect of decreasing swirler angle of the main injection elements is an increase in the thickness of the shear layers between the outer main elements and the central pilot element.

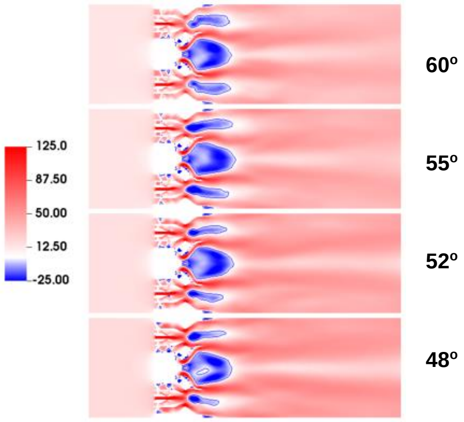

Figure 4. OpenNCC Contours: Axial flow velocity (m/s) for four swirler passage angles (Reacting flow)

Figure 5 shows a composite summary of the predicted mid-plane contours of fuel-air ratio (FAR), combustor temperature and NO mass-fraction for the four swirler configurations computed with the OpenNCC. The predicted contours of FAR show that the pilot injector strongly dominates the flame development near the dome of the combustor. The very high FAR behind the pilot is a combined effect of (a) the relatively strong recirculation zone created by a 'high-swirl pilot design' [Ajmani 2016], and (b) the relatively faster fuel evaporation due to better fuel-air mixing created by the pressure atomizer of the pilot element. The presence of regions of stoichiometric burning behind the pilot element of each of the four designs results in the presence of a high temperature core pilot region surrounded by a relatively cooler flame region behind the main injectors. The main injection elements, with relatively weaker recirculation zones and pre-filming air-blast type fuel injectors with relatively slower evaporation, exhibit significantly cooler flame structures as compared to the pilot element. As expected, the high-temperature regions of the pilot element make the dominant contributions to the NO mass-fraction production for each of the four swirler designs.

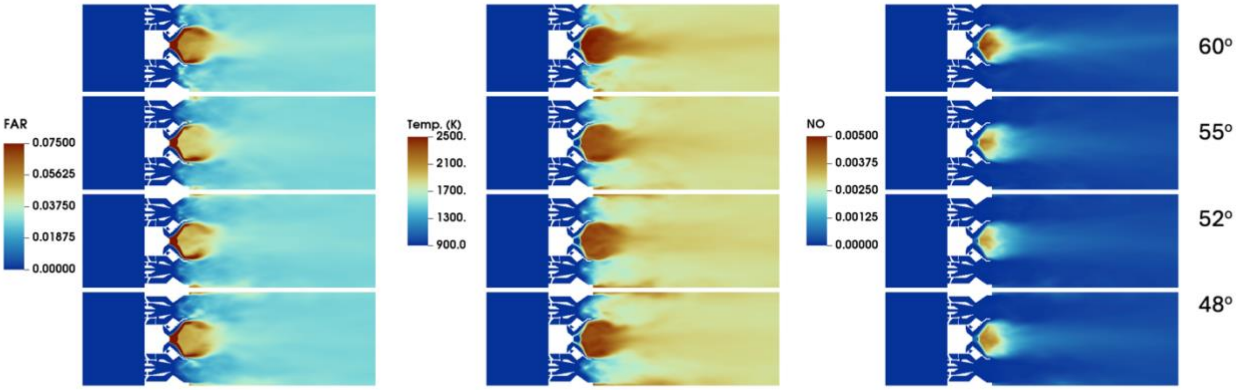

Figure 5. OpenNCC Contours at mid-plane section: FAR (left), Temperature (center) and NO mass fraction (right) for four different swirler passage angles

Figure 6 shows details of the development of axial velocity (V_{ax}), temperature (T), FAR and NO mass-fraction at two axial cross-sections near the dome face of the combustor. The pilot element at the dome cross-section shows much stronger recirculation zones, flame temperatures, FAR and NO, as compared to the six surrounding main injection elements. At the dome, the 55° and 52° designs have lower values of local FAR behind the pilot as compared to the higher values seen behind the pilot of the 60° design. The effect of the largest swirler angle (60°) design is to produce the strongest recirculation at the exit of the main injector venturis, which leads to the highest local temperature, FAR and NO at the dome face for this particular configuration. As the flow proceeds to the 1.0in (25.4mm) location downstream, all four designs lose their recirculation zones behind all the seven injection elements. The temperature profiles behind the main injectors show the development of local hot spots, one for each main injector, near the combustor walls. The local temperature, FAR and NO near each hot spot increases as the swirler angle decreases. The physical explanation for this behavior is that the higher swirler angle main injection elements produce relatively stronger local flames, which offer greater resistance to being pushed radially outwards towards the walls. The fastest downstream mixed-out temperature and lowest attendant NOx could thus be expected from a design which can mitigate the strong influence of the pilot injector on the main injectors.

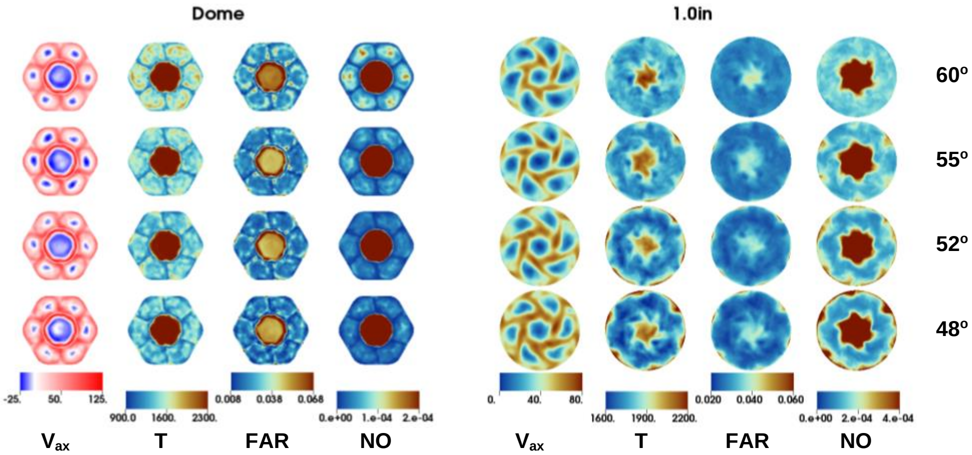

Figure 6. OpenNCC Contours at mid-plane section: FAR (left), Temperature (center) and NO mass fraction (right) for four different swirler passage angles

The flow features at two additional cross-sections, 4.0in (101.6mm) and 6.0in (99% or 150mm) downstream of the dome are shown in Figure 7. The trend of hot combustion products from the main injectors impinging upon the outer walls and producing increased NOx, particularly for the 52° and 48° swirler designs, peaks at the 4.0in cross-section. The pilot element average temperature, FAR and NOx, seen at the center of the 4.0in section, is almost 50% less than that at the 1.0in section (see fig.6). The 55° design is shown to have the least cross-sectional variance in all four flow quantities at the 4.0in downstream location. The set of results shown at the 99% (or 6.0in) location represents the exit temperature (T_4), exit FAR and exit NO mass fraction used for computing the area-averaged quantities that served as inputs for the EINOx (g of NOx per kg of fuel) comparisons for the four designs.

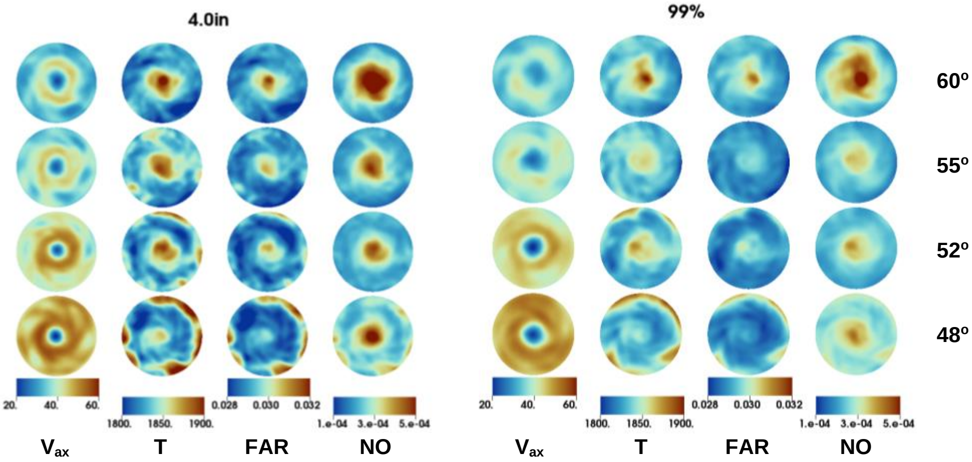

Figure 7. OpenNCC Contours at mid-plane section: FAR (left), Temperature (center) and NO mass fraction (right) for four different swirler passage angles

The respective predicted trends of NO production by the central pilot element and by the six main elements for the four computed designs are summarized as:

- NO production by the center PILOT is very similar for all 4 swirler designs; slightly higher for 60°
- NO production behind MAINS at dome: 60° > 55° > 48° > 52°
- NO near combustor wall at 1.0in and further downstream of dome : 48° > 52° > 55° > 60°

A summary of the OpenNCC results for the supersonics cruise condition used in the current parametric study of is shown in Table 3. In order to ensure that all four computational cases met the CFD convergence criteria of uniform area-averaged temperature and area-averaged FAR at the exit plane of the computational domain, a comparison was made also made with the 'CFD target' value of T_4 and 'metered' FAR. The 'CFD target' T_4 was computed from input T_3 =884K and 'metered' FAR = 0.0295 (based on CFD inputs of air and fuel flow rates). The computed FAR was obtained by performing a gas analysis of combustion products at the exit plane. The EINOx values at the exit plane were computed from the computed NO (ppm) and FAR at the exit plane (EINOx = NO*(1+1/FAR)*46/30).

Table 3. Effective areas (AC_d) of various airflow passages of four different single-cup designs (normalized by the effective area of the six mains elements of the 52° configuration)

Swirler Angle (Six Main Elements)	Computed T_4 (K)	Computed FAR (gas analysis)	Computed NO (ppm)	EINOx (g/kg of fuel)
60° (Co-Rotating)	**1837**	**0.0293**	**300**	**15.8**
55° (Co-Rotating)	**1836**	**0.0289**	**242**	**12.6**
52° (Co-Rotating)	**1834**	**0.0288**	**225**	**12.3**
48° (Original design, Co-Rotating)	**1840**	**0.0290**	**295**	**15.6**
CFD Target (based on input T_3, metered FAR)	**1840**	**0.0295**	**-**	**-**

The area-averaged computed T4 and FAR at the exit plane, as time-averaged over the final flow through time of 5ms for all four designs, showed excellent agreement with the CFD Target values of T4 and FAR respectively. The converged values of EINOx for the four designs, and their respective distribution in the combustor are summarized below:

- All four swirler designs were predicted to have > 99% combustion efficiency and negligible EICO at the exit.
- All four swirler designs had similar, very high NO production by the central pilot swirler
- The EINOx contribution of the pilot swirler at the combustor exit plane was significantly influenced by the stability and size of the recirculation zones of the six outer main swirlers. The EINOx distribution at the exit was dominated by the pilot, particularly for 60° design, and shifted towards the combustor wall for the 48° design.

The final down-selection of two out of three candidate designs was based on a combination of the lowest EINOx values, the circumferential distribution of the NO mass-fraction along the various axial locations of the combustor, and the overall stability of the reacting flowfield downstream of the combustor dome. A summary of the rationale for the selection of the 55° and 60° design is given below:

- 52° and 55° co-rotating swirler designs both had ~20% lower EINOx as compared to the 48° and 60° swirler designs. From a liner cooling perspective, the 55° design was preferable to the 52° design which had much higher impingement of combustion products and hot spots on the combustor wall.
- 60° design selected was for (a) potential to successfully perform fuel-staging between pilot and main injection elements to reduce EINOx, (b) much lower liner cooling flow requirement at combustor walls as compared to the 52° design even though the latter had 20% lower predicted EINOx
- In follow-up computations with the OpenNCC, EINOx for the 60° swirler design was shown to be reduced by 10% over the equal-FAR approach. The fuel-staging approach was performed by reducing the pilot element FAR by 24% and increasing the FAR for each of the six main injection elements by 4%, respectively.

4.0 Summary and Significance

The impact on NOx emissions of swirler angle variations of six main swirlers of a seven-element lean-direct injection (LDI) module was studied at a supersonic cruise condition for NASA's Commercial Supersonic Technology program. The Open version of the National Combustion Code (OpenNCC) was used to perform two-phase reacting flow computations with an 'average' Jet-A (A2) fuel. The best Low NOx injector in the parametric study of four different swirler designs was predicted to have 20% lower NOx than the baseline swirler design. Two of the four designs evaluated in the current CFD study with the OpenNCC were down-selected for 3-D manufacturing and testing in NASA Glenn Research Center's CE-13C combustion facility. The test data results of EINOx for the 60° and 55° swirler designs identified for combustion testing by the current CFD study will be compared with the pre-test CFD predictions. Future Low NOx injector design efforts will continue to leverage the CFD capabilities of the OpenNCC code and the combustion test facilities at NASA GRC to help the CST project reach its cruise NOx emissions goals.

5.0 Acknowledgements

This research was funded by the Commercial Supersonic Technology (CST) Project under NASA's Advanced Air Vehicles Project (AAVP). Computational resources were provided by the NAS Supercomputing at NASA Ames Research Center.

6.0 References

[1] Ajmani, K., and Chang, C.T., "CFD Evaluation of Aviation Fuels for Commercial Supersonics Technology," AIAA Paper 2022-1105, AIAA Scitech Meeting 2022, January 2022, San Diego CA.

[2] Tacina, K.M., Podboy, D.P., Lee, P., and Dam, B., "Gaseous Emissions Results from a Three-Cup Flametube Test of a Third-Generation Lean Direct Injection Combustor Concept", ISABE 2017, Edinburgh UK

[3] Ajmani, K., Lee, P., Chang, C.T. and Kudlac, M.T., "CFD Evaluation of Lean-Direct Injection Combustors for Commercial Supersonics Technology," AIAA Paper 2019-4199, AIAA Propulsion and Energy Conference 2019, July 2019, Indianapolis IN.

[4] Ajmani, K., Lee, P., Mongia, H.C. and Tacina, K.M., "CFD Predictions of N+3 Cycle Emissions for a Three-Cup Gas Turbine Combustor," AIAA Paper 2018-4957, 54th AIAA Joint Propulsion Conference, July 2018, Cincinnati OH.

[5] Ajmani, K., and Moder, J.M., "CFD Evaluation of Sustainable Aviation Fuels for Commercial Supersonics Technology," 13th US National Combustion Meeting, Paper 180AFE-0190 March 2023, College Station TX.

[6] Ajmani, K., and Chang, C.T., "CFD Evaluation of Aviation Fuels for Commercial Supersonics Technology," AIAA Paper 2022-1105, AIAA Scitech Meeting 2022, January 2022, San Diego CA

[7] Shih, T. H., Liu, N. S., 2008, "Modeling of internal reacting flows and external static stall flows using RANS and PRNS," Flow Turbulence and Combustion: **81**: pp. 279–299.

[8] M.S. Raju, "LSPRAY-IV: A Lagrangian Spray Module," NASA CR-2012-217294.

[9] H. Wang, R. Xu, K. Wang, C.T. Bowman, D.F. Davidson, R.K. Hanson, K. Brezinsky, F.N. Egolfopoulos, A physics-based approach to modeling real-fuel combustion chemistry - I. Evidence from experiments, and thermodynamic, chemical kinetic and statistical considerations, *Combustion and Flame* 193 (2018) 502-519.

[10] Liou, M.-S, 2006, "A Sequel to AUSM, Part II: AUSM+-up for All Speeds," Journal of Computational Physics: 214: pp.137-170.

[11] Muralidharan, B., Zambon, A., Hosangadi, A., Calhoon, W. H. Jr, 2018, "Application of a progress variable based approach for modeling non-premixed/partially premixed combustion under high-pressure conditions," Proceedings of the AIAA Joint Propulsion Conference 2018, July 2018, Cincinnati OH, AIAA Paper 2018-4560.

[12] Zambon, A. C., Muralidharan, B., Hosangadi, A., Ajmani, K., 2020, "A Multi-Time-Scale Flamelet Progress Variable Approach in OpenNCC for Predicting NOx Applied to Commercial Supersonic Transport Combustor Designs," Proceedings of the AIAA Propulsion and Energy Forum, August 2020, virtual, AIAA Paper 2020-3896.

[13] Ajmani, K., Moder, J. P., 2024, "CFD Evaluation of Radial Airflow Lean Direct Injectors for Commercial Supersonics Technology," Proceedings of 2024 Spring Technical Meeting of the CSSCI, May 2024, Cleveland OH,

Paper 235AFEQ-0036.

[14] David G. Goodwin, Harry K. Moffat, Ingmar Schoegl, Raymond L. Speth, and Bryan W. Weber. *Cantera: An object-oriented software toolkit for chemical kinetics, thermodynamics, and transport processes*. https://www.cantera.org, 2022. Version 2.6.0. doi:10.5281/zenodo.6387882

[15] Lucas Esclapez, Peter C. Ma, Eric Mayhew, Rui Xu, Scott Stouffer, Tonghun Lee, Hai Wang, Matthias Ihme, "Fuel effects on lean blow-out in a realistic gas turbine combustor," *Combustion and Flame*, 181 (2017). https://dx.doi.org/10.1016/j.combustflame.2017.02.035

[16] Teddy D. Blacker, Steven J. Owen, Matthew L. Staten, William R. Quadros, Byron Hanks, Brett W. Clark, Ray J. Meyers, Corey Ernst, Karl Merkley, Randy Morris, Corey McBride, Clinton Stimpson, Michael Plooster, and Sam Showman. *CUBIT Geometry and Mesh Generation Toolkit 15.2 User Documentation*. United States: N. p., 2016. Web. https://doi.org/10.2172/1457612

[17] Hank Childs, Eric Brugger, Brad Whitlock, Jeremy Meredith, Sean Ahern, David Pugmire, Kathleen Biagas, Mark Miller, Cyrus Harrison, Gunther H. Weber, Hari Krishnan, Thomas Fogal, Allen Sanderson, Christoph Garth, E. Wes Bethel, David Camp, Oliver Rubel, Marc Durant, Jean M. Favre, and Paul Navr, "VisIt: An End-User Tool for Visualizing and Analyzing Very Large Data," *High Performance Visualization--Enabling Extreme-Scale Scientific Insight (2012), 357-372.*